# High-Performance Transparent Broadband Microwave Absorbers

*Heyan Wang, Yilei Zhang, Chengang Ji, Cheng Zhang, Zhengang Lu,\* Yunfei Liu, Zhibo Cao, Jing Yuan, Jiubin Tan, and L. Jay Guo\**

The ability to absorb a broad frequency range of microwaves is essential for improving the performance of various electromagnetic interference shielding applications. However, the achievement of broadband microwave absorption with high optical transparency remains a long-standing and unsolved challenge. Here, a simple and powerful method for high-efficiency broadband microwave absorption is presented by introducing strongly overlapped multi-cavity resonances, which is supported by multi-layer structures comprising of alternating graphene/silica pairs and ultrathin silver films. A design guideline for achieving broadband absorption in multi-layer structures is proposed and, more importantly, the complementary effect of different graphene layers on the microwave absorption mechanism is revealed for the first time, providing a new analytical perspective. Experiments show that the absorption efficiency of the proposed multi-layer structures is near unity (≈100%) at resonant peaks with absorption bandwidths (≥50%) up to ≈30 GHz within the measured range of 32 GHz. In addition, the multi-layer structures exhibit highly visible transmittance ranging from ≈85.8% to 68.0%. The proposed general theoretical framework and physical insights in combination with experimental demonstrations lay the foundation for designing a new type of transparent broadband microwave absorber.

## 1. Introduction

Microwave absorbers play a key role in the current explosive development of wireless and highly integrated electronics, which can eliminate electromagnetic radiation and enhance energy utilization efficiency.[1–5] In recent years, there has been a surge of interest in the development of optically transparent microwave absorbers, which are necessary components in numerous applications, such as electromagnetic interference (EMI) shielding windows and domes for aircraft, displays, panels of instruments, and optical detecting/monitoring devices used in medical and electronic safety areas.[6–10] The development of high-performance transparent microwave absorbers has been a long-standing but critical challenge, and the desired features include high optical transmittance, powerful microwave-absorbing capability, and wide operating bandwidth.[11,12] Unfortunately, these requirements are not adequately satisfied by current microwave shielding or absorbing methods and materials.

Extensive research has been devoted to exploiting transparent microwave absorbers using metamaterial and metasurface absorbers, in which subwavelength building blocks are artificially arranged in 3D configurations or at 2D interfaces.[13–16] By tailoring the effective permittivity and permeability of metamaterials to match the impedance with free space, the absorbers can offer excellent microwave absorption. For example, metamaterials or metasurface absorbers based on standing-up closed-ring resonators,[17] loop-dielectric multi-layered structures, tapered metal-dielectric structures, and bow-tie array metal mesh structures have shown the ability to absorb electromagnetic waves with high efficiency at the desired frequencies.[18–20] Meanwhile, various schemes based on patterned indium tin oxide (ITO) or other transparent conducting film structures have demonstrated the capability to broaden the microwave absorption by rationally designing resonant modes with different unit cells.[21–23] These artificial structures require complicated fabrication procedures involving multiple steps of photolithography and etching, and the low visible transparency of the ground layer further hinders their optical applications.

H. Wang, Y. Zhang, Z. Lu, Y. Liu, Z. Cao, J. Yuan, J. Tan
Ultra-precision Optical & Electronic Instrument Engineering Center
Harbin Institute of Technology
Harbin 150001, China
E-mail: luzhengang@hit.edu.cn
H. Wang, Y. Zhang, Z. Lu, Y. Liu, Z. Cao, J. Yuan, J. Tan
Key Lab of Ultra-precision Intelligent Instrumentation
(Harbin Institute of Technology)
Ministry of Industry and Information Technology
Harbin 150080, China
C. Ji, L. J. Guo
Department of Electrical Engineering and Computer Science
University of Michigan
Ann Arbor, MI 48109, USA
E-mail: guo@umich.edu
C. Zhang
School of Optical and Electronic Information & Wuhan National
Laboratory for Optoelectronics
Huazhong University of Science and Technology
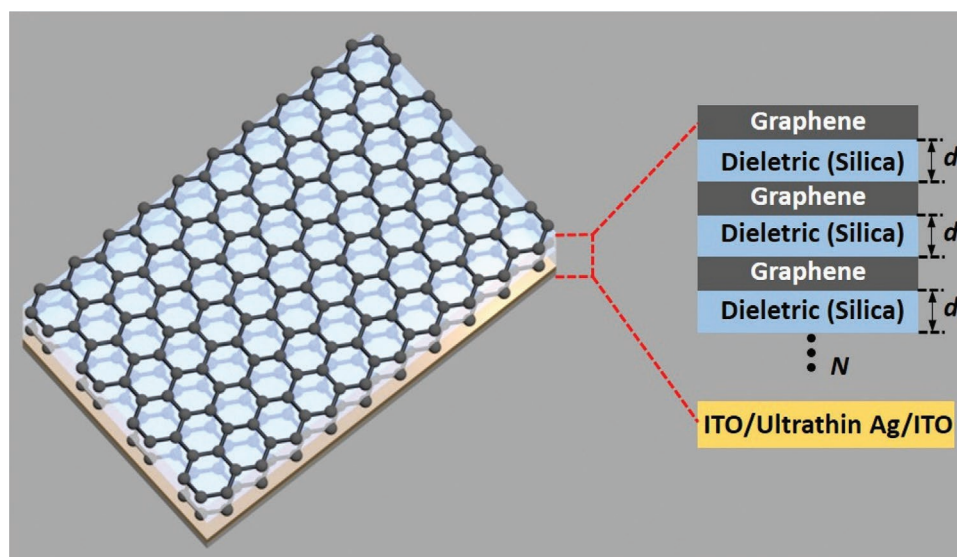Wuhan 430074, China

**Figure 1.** Schematic representation of the proposed transparent broadband microwave absorber consisting of multiple graphene/silica units and ITO/ultrathin Ag/ITO.

Other studies have focused on the implementation and integration of atomically thin graphene to construct transparent microwave absorbers owing to their extraordinary optoelectronic properties, such as high electron mobility and ultra-low optical loss.[24–27] Graphene-based microwave absorbers include monolayer to multi-layer graphene,[28,29] graphene-based composites,[30] patterned graphene with transparent spacers, and graphene hybrid structures such as graphene/polyethylene terephthalate (PET), graphene/polymethyl methacrylate (PMMA), and graphene/silica multi-layer stacks,[31–35] all exhibiting favorable attenuation bandwidth; however, the microwave absorption has not been significantly improved at the expense of overall transparency. Therefore, the full potential of graphene has not yet been achieved.

Inspired by hyperbolic metamaterials based on alternating graphene structures,[36–38] that exhibit many unusual properties, such as strong enhancement of spontaneous emission and negative refraction, we are motivated to investigate how to enhance microwave absorption over a broad spectrum of microwave frequencies using multi-layer structures. In this study, we theoretically and experimentally demonstrate a high-performance transparent broadband microwave absorber composed of multiple graphene/silica units and an ultrathin silver film (MGSS). Using simple building blocks of graphene/silica units to replace the 3D/2D array of subwavelength elements in classical metamaterials/metasurfaces, we present a simple and powerful methodology for achieving broadband microwave absorption by introducing multi-cavity resonances, which also show a slow downward trend from peak absorption by rational design. Furthermore, the resonant peaks and overall bandwidth can be readily tuned by altering the number of graphene/silica units and dielectric thicknesses. To date, excellent research of broadband microwave absorbing materials based on MXenes and graphene-based composites has been investigated,[39–41] however, they are totally opaque; here we aimed to achieve optically transparent microwave absorbers using multi-layer structures, paving the way for practical applications in optical areas.

## 2. Results and Discussion

### 2.1. Proposed Broadband Microwave Absorber

**Figure 1** shows a schematic diagram of the proposed transparent microwave absorber, where multiple graphene/silica pairs were placed on top of an ultrathin silver (Ag) film to construct microwave cavities, featuring broadband microwave absorption, high transparency, and strong EMI shielding capability. The number of graphene/silica units $N$ and the dielectric thickness $d$, that is, the silica thickness in this case, can be tuned according to different application requirements. Owing to its outstanding visible transparency and partial microwave absorption and transmission over a broad range of frequencies, monolayer graphene was selected as the microwave absorbing medium. An ultrathin Ag film (<10 nm) with an ultra-smooth and continuous surface, which was fabricated by co-sputtering a small amount of copper during the Ag deposition process, was chosen as the bottom microwave reflecting layer in the multi-layer structure because of its low optical loss in the visible wavelength range and high electrical conductivity simultaneously.[42–44] Considering the percolation threshold of thickness to form a continuous and smooth film by the co-sputtering method, we selected an 8-nm-thick doped Ag film to ensure its excellent optoelectronic performance. Furthermore, to enhance the visible transmittance of ultrathin Ag, 40-nm-thick ITO undercoat and overcoat layers were used as optical antireflection coatings.

The as-grown monolayer graphene and ultrathin Ag films were characterized using scanning electron microscopy (SEM) and X-ray photoelectron spectroscopy (XPS), as shown in **Figure 2**. The clear folds at different scales in Figure 2a further
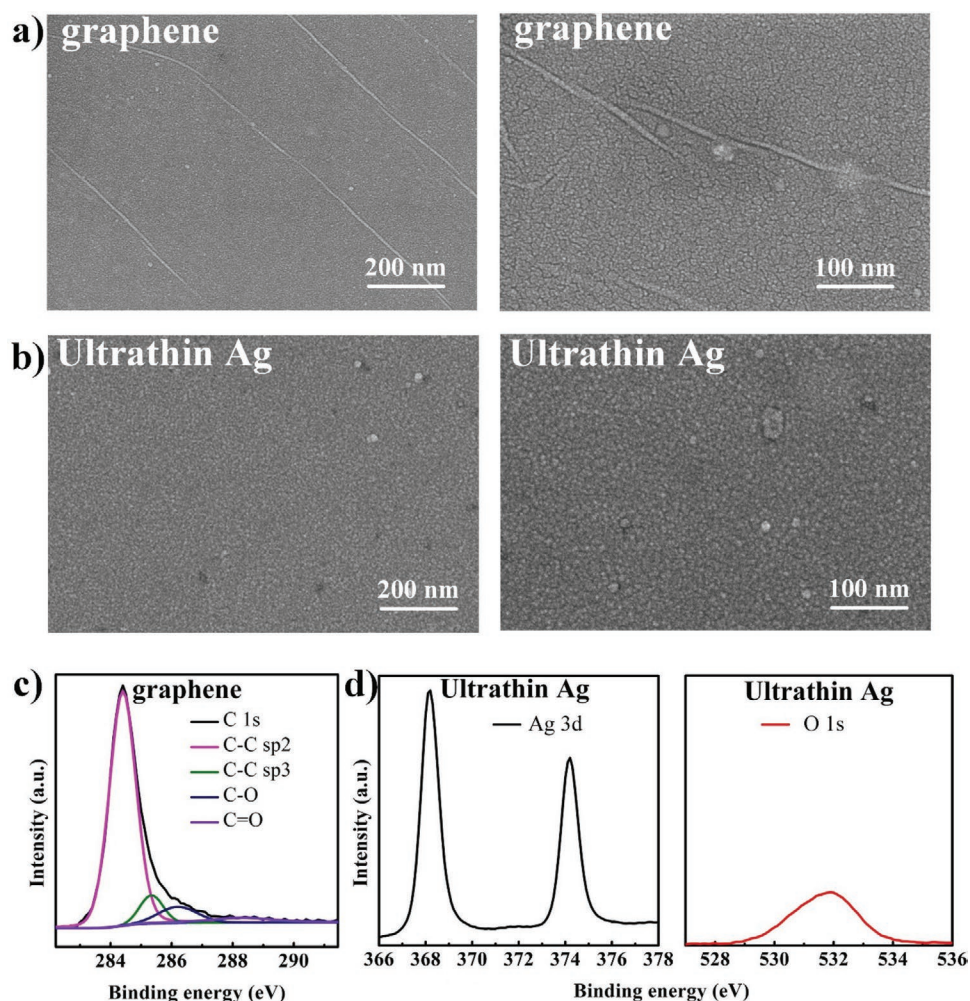
**Figure 2.** SEM images of a) chemical vapor deposition (CVD)-grown monolayer graphene and b) ultrathin Ag. XPS measurement results of c) monolayer graphene and d) ultrathin Ag.

indicate the presence of graphene. In addition, the SEM images of ultrathin Ag show a continuous and smooth surface feature, which indicates the high quality of the deposited metal film. As can be observed from XPS results, Figure 2c shows the deconvoluted C 1s spectra of the graphene film on the silica substrate. The C1s peak corresponding to the sample consists of four components, one at binding energy of 284.4 eV which features the C−C sp2 bonds, one at 285.3 eV which is attributed to carbon bonds with sp3 hybridization and two components at binding energy of ≈286.2 and 288.3 eV which correspond to C−O and C=O bonds, respectively.[45,46] However, the intensity of the C 1s core level peak centered at 284.4 eV is much higher than the other three peaks (>10:1), indicating the high-quality of graphene film with a small amount of oxidized carbon contamination due to surface chemi-absorption.

For ultrathin Ag film, in Figure 2d, Ag 3d and O 1s peaks can be detected by XPS. Owing to the surface oxidation of ultrathin Ag film, the O 1s at the binding energy of 531.8 eV can be probed on the sample surface. After checking Ag 3d peaks, in terms of the binding energy of AgO (367.4 eV), AgO$_2$ (367.8 eV), and Ag (368.2 eV), respectively, the as-deposited ultrathin Ag

film mainly contains the Ag and a small amount of AgO on the surface.[47] Furthermore, as evidenced by the presence of several diffraction peaks, the X-ray diffraction angular spectrum (Figure S2, Supporting Information) reveals that ultrathin Ag film is polycrystalline.

It is important to mention that other materials can be used to replace graphene (e.g., by carbon nanotubes or MXenes), silica (e.g., by other transparent dielectrics, like PET or PMMA), and ultrathin Ag (e.g., by metallic mesh or metal nanowires) to construct the multilayer structures, and the method can be further extended to a more generalized case.

## 2.2. Microwave Absorption Performance and Design Guideline

We established a detailed multi-layer structure calculation model based on the transfer matrix method (TMM), which is illustrated in Section 1.1, Supporting Information. Important parameters, including the number of units, dielectric constants, and dielectric thickness, were involved in optimizing the microwave absorber. As the dielectric constants of the materials in each
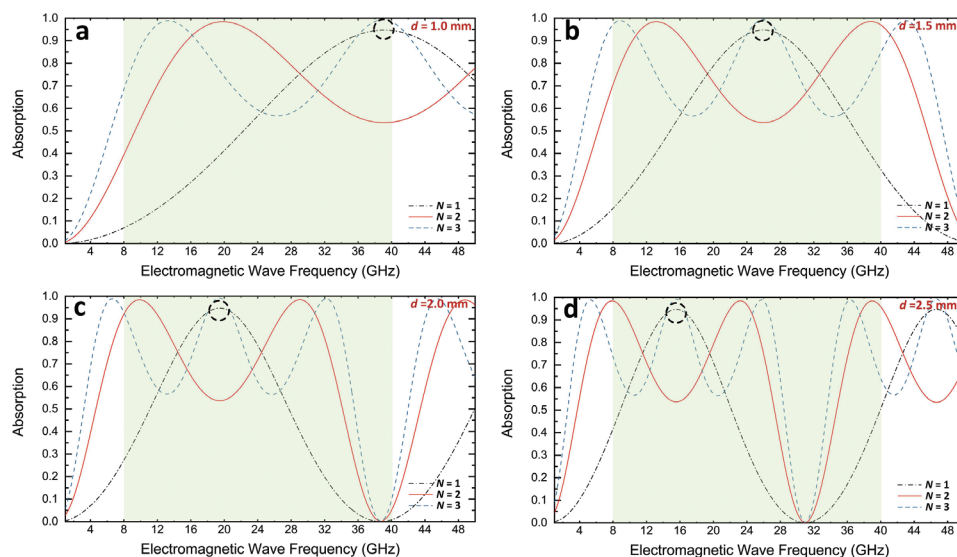
**ADVANCED
SCIENCE NEWS**
www.advancedsciencenews.com

**ADVANCED
MATERIALS
INTERFACES**
www.advmatinterfaces.de

**Figure 3.** Calculated microwave absorption of the proposed MGSS as a function of electromagnetic wave frequency from 1 to 50 GHz with different number of graphene/silica units ($N$ = 1, 2, 3) at different dielectric thicknesses. a) $d$ = 1.0 mm. b) $d$ = 1.5 mm. c) $d$ = 2.0 mm. d) $d$ = 2.5 mm.

layer (graphene, silica, and ultrathin Ag) were fixed, it can be anticipated that the microwave absorption performance can be tuned by varying the number of units $N$ and dielectric thickness $d$ in the units. To gain a thorough understanding of how variations in the number of units $N$ and dielectric thickness $d$ affects the microwave absorption behaviors, $N$ was varied from 1 to 3 and $d$ was varied from 1.0 to 2.5 mm in the calculation. Considering the microwave absorption, that is, $A = 1 - R - T$, where $R$ represents the reflectance and $T$ represents the transmission, the microwave absorption can be obtained from $R$ and $T$.

First, it is clear that under the same dielectric thickness in **Figure 3**a–d, the absorption bandwidth ($A \geq 50\%$) becomes broader as the graphene/silica unit quantities change from $N = 1$ to $N = 3$. For the single graphene/silica unit case ($N = 1$), the highly efficient absorption position is limited to a relatively narrow band around the resonant frequency, and it gradually extends to more peaks when $N$ increases. In Figure 3b, when $d$ is fixed to 1.5 mm, the absorption bandwidth of the structure increases from 28 GHz ($N = 1$) to 39 GHz ($N = 2$), up to 44 GHz ($N = 3$) in the overall 50-GHz band. As shown in Figure 3b, the proposed MGSS ($d$ = 1.5 mm, $N = 3$) exhibits an excellent absorbing performance with high efficiency, which arises from three distinctive absorption resonances appearing at ≈9, 26, and 44 GHz positions. From Figure 3b–d, it is interesting to note that the number of resonant peaks shows a proportional relationship with the number of the units; therefore, adding the graphene/silica units would generate more absorption peaks in the concerned band, and the overlap of these peaks at nearby frequencies helps improve the absorption efficiency and widen the bandwidth.

Second, when $N$ is fixed, it is apparent that the absorption resonances shift toward the lower frequency region with increasing silica thickness $d$. For instance, when we observe the different curves at $N = 1$, the first resonant peak (marked by the dotted circles) moves from 39 GHz ($d$ = 1 mm) to 15.5 GHz ($d$ = 2.5 mm). In fact, the dielectric thickness influences the propagation phase, and a thicker dielectric would result in a

larger phase accumulation, which requires a longer resonant wavelength (lower frequency) to achieve the destructive interference condition for the reflected waves. More importantly, we note that the reduced thickness of silica contributes to a broader absorption bandwidth at the same $N$, for example, the bandwidth increases from 16 GHz ($d$ = 2.5 mm) to 28 GHz ($d$ = 1.5 mm) at $N = 1$, and a similar trend can be found at $N \geq 2$. Finally, at the same total dielectric thickness, more graphene/silica units lead to a broader bandwidth. As compared in Figures 3a,c, the absorption bandwidth of MGSS at $d$ = 1.0 mm, $N = 2$ shows an over-20 GHz wider than that of $d$ = 2.0 mm, $N = 1$, which directly illustrates the effect of introducing more units even at the same totally dielectric thickness.

Generally, based on the above results, the calculated spectra show that the optimized multi-layer structure results from the small dielectric thickness $d$ with more units $N$, which is also the proposed design guideline for achieving broadband microwave absorption. In essence, a relatively small phase thickness of the dielectric is selected to lower the quality factor of the single resonance, thus slowing down the descent rate from the resonant peaks, and more units are selected to create and combine these absorption resonances, which intuitively improves the absorption bandwidth. The best simulated result exhibits a maximum bandwidth ($\geq 50\%$) of 44 GHz from 1 to 50 GHz, covering the entire radar band, with a peak absorption of over 90% ($d$ = 1 mm, $N = 3$ in Figure 3a).

To verify the microwave absorption performance, we constructed MGSS with different unit numbers and silica thicknesses using monolayer graphene and ultrathin Ag configured as simulations. **Figure 4**a–d depicts the measured absorption results using the waveguide measurement method (Figure S3, Supporting Information) ranging from 8 GHz to 40 GHz covering the X, Ku, K, and Ka bands. $R$ and $T$ were retrieved from the measured parameters, $S_{11}$ and $S_{21}$. Owing to the high electrical conductivity of ultrathin Ag film, it ensures little microwave transmission through the multi-layer structures ($T \approx 0$). The measured shielding effectiveness of the MGSS at different
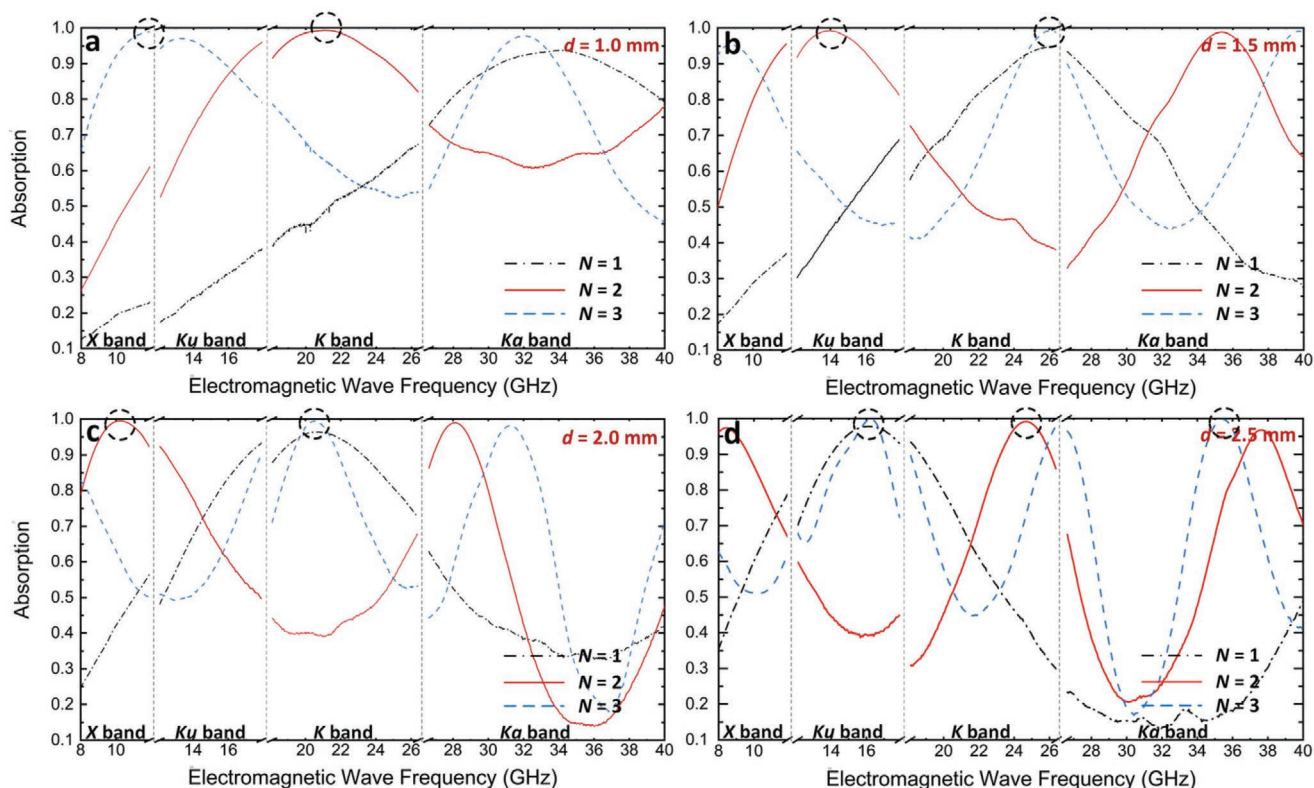
**ADVANCED
SCIENCE NEWS**
www.advancedsciencenews.com

**ADVANCED
MATERIALS
INTERFACES**
www.advmatinterfaces.de

**Figure 4.** Measured microwave absorption of the proposed MGSS using waveguide measurement method as a function of electromagnetic wave frequency covering the X, Ku, K, and Ka bands from 8 to 40 GHz with different number of graphene/silica units ($N$ = 1, 2, 3) at different dielectric thicknesses. a) $d$ = 1.0 mm. b) $d$ = 1.5 mm. c) $d$ = 2.0 mm. d) $d$ = 2.5 mm.

configurations was ≈27 dB (Figure S4, Supporting Information), exhibiting a strong EMI shielding capability.

It is clear that the absorption results at neighboring frequencies between two adjacent radar bands could not perfectly connect, mainly because of the different graphene samples used in different bands to fit the size of the waveguides, therefore the curves are slightly discontinuous. However, the overall trends and resonant peaks agree well with the calculated ones (blue shaded areas in Figure 3a–d), further validating the correctness and effectiveness of the calculation model. Considering MGSS ($d$ = 1.5 mm, $N$ = 3) as an example, the experimental results show that three resonant peaks appeared at ≈9, 26, and 40 GHz, corresponding well with the simulated results.

It is important to note that nearly perfect absorption ($A$ ≈100%) is achieved for the MGSS at different configurations in Figure 4a–d (marked by dotted circles), proving that critical coupling for different multi-layer structures is achieved and exhibits great potential for high-performance microwave absorption. Specifically, according to the experiments in Figure 4c, 95%, 99.5%, and 99% of maximum absorption for $N$ = 1, 2, and 3 at 2-mm-thick silica were obtained at ≈21, 10, and 21 GHz, respectively. In addition, it is verified from the figures that by increasing the number of graphene/silica units $N$ and decreasing the silica thicknesses, a broader measured bandwidth could be obtained. The best absorption bandwidth for MGSS ($d$ = 1 mm, $N$ = 2 and $d$ = 1 mm, $N$ = 3 in Figure 4a) is ≈30 GHz within the 32 GHz band, which is limited by the

measurement frequency range, however still shows great consistency with the calculation. The measured absorption spectra have a relatively narrower profile than the calculated results owing to the refractive index parameter discrepancies between the modeled graphene/ultrathin Ag and samples in the actual structure, which are slightly different from the bulk data.

## 2.3. Broadband Microwave Absorption Mechanisms

To investigate the broadband microwave absorption mechanisms, we established a numerical model to calculate the electric field intensity profiles in the multi-layer structures at the frequencies of concern through TMM; the detailed calculation model is illustrated in Section 1.2, Supporting Information. **Figure 5** displays the normalized electric field intensity distributions as a function of the frequency within the structures at different number of units $N$ and dielectric thicknesses $d$. In particular, to better illustrate the field distribution regions in the graphene layers, the thickness of each graphene layer was not drawn to scale. Comparing the upper and lower calculated results at the same $d$, the cavity resonance modes inside the structure increase from $N$ = 2 to $N$ = 3. The strong electric field in each subgraph is primarily confined in the silica layers (as marked by dotted circles) between the graphene, arising from fundamental and high-order Fabry-Pérot cavity resonance modes, and they appeared at the same frequency positions
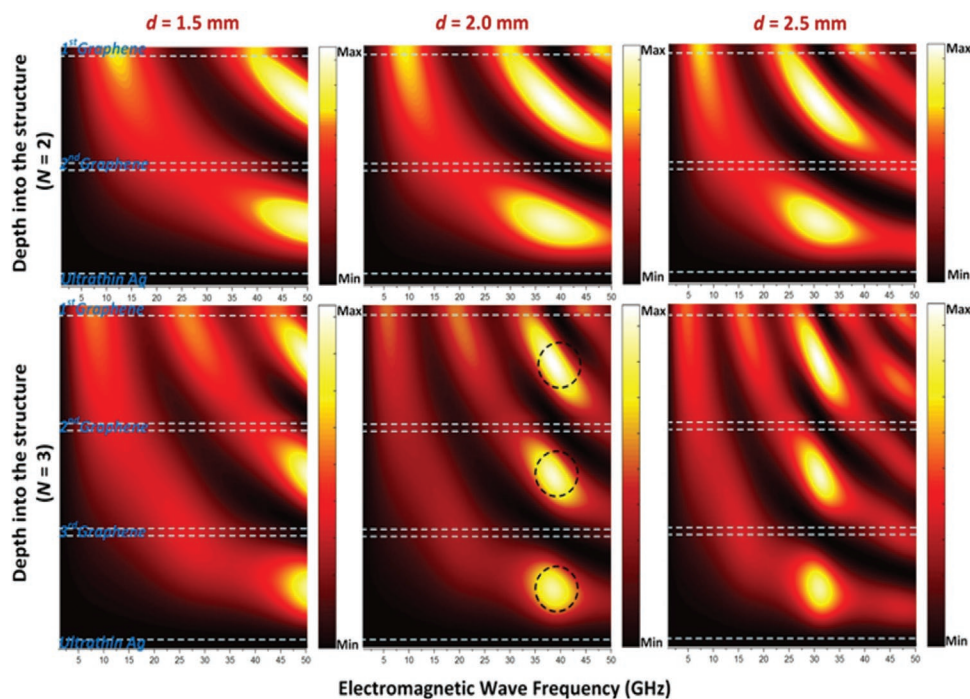
**Figure 5.** Simulated electric field intensity profiles in the structures with different dielectric thicknesses from $N = 2$ to $N = 3$ at concerned frequencies.

within different silica layers because the multi-layer structure was completely symmetric. As shown in Figure 5, the electric field in the first graphene layer is more intensively focused compared to that in the second and third graphene layers, and is extremely weak in the bottom ultrathin Ag layer, ensuring minimum microwave transmission through the structure.

To verify the origin of these cavity resonances, the net phase shift in the dielectric layers (i.e., silica) of MGSS is calculated as a function of frequency, which involves two phase shifts occurring upon the reflection from the interfaces and the propagation phase accumulation within the layer. The propagation phase accumulation can be obtained using Equation (1), while the phase shift from the reflection occurring at the two interfaces can be retrieved from the reflection coefficient $\overline{r}_k$ by Fresnel's law using Equation (2):

$$\varphi_{\text{prop}} = \frac{4\pi}{\lambda} nd \cos\theta \tag{1}$$

$$\overline{r}_k = \frac{r_k + r_{k+1}\exp(i\delta_k)}{1 + r_k r_{k+1}\exp(i\delta_k)}, \, r_k = \frac{m_k - m_{k-1}}{m_k + m_{k-1}}, \, \varphi_{ref} = \arg(\overline{r}_k) \tag{2}$$

where $\lambda$ represents the incident microwave wavelength, $n$ represents the refractive index of silica, $d$ represents the layer thickness, $\theta$ represents the wave propagation direction, and is zero for normal incidence in the calculation case, $m_k$ represents the complex refractive index of the $k^{\text{th}}$ layer material, and $\phi_{\text{ref}}$ represents the argument of $\overline{r}_k$. According to the calculation, the cavity resonances in each silica layer correspond to the positions where the net phase shifts are equal to a multiple of $2\pi$, further revealing that the fundamental and high-order

Fabry-Pérot cavity resonance modes are excited at these frequencies. In simple physics, at resonances, microwave beams reflected from the air/graphene and silica/Ag interfaces are canceled out by destructive interference; consequently, the reflection of the structure is profoundly suppressed. The interference condition is associated with single or multiple round-trip phase shifts of the electromagnetic waves inside the resonant cavity. The variation in reflection at various frequencies is because of the different phase delays of the frequencies as well as the material dispersion.[48,49]

**Figure 6** shows the calculated energy absorption map at different frequencies within the multi-layer structures (Section 1.2, Supporting Information), clearly indicating that most of the incident energy is absorbed by the graphene layers in the MGSS. By comparing with the corresponding calculated results in Figure 5, the energy absorption in different layers (graphene, silica, and ultrathin Ag) at different configurations is directly proportional to the electric field intensity $E$ (Absorption$(x) = 2\pi\varepsilon_0 n\kappa f|E(x)|^2$, where $f$ represents the wave frequency, $\varepsilon_0$ represents the permittivity of free space, and $n$ and $\kappa$ represent the refractive index and extinction coefficient of the materials, respectively. Therefore, the absorption resonance positions appear at frequencies where the electric field is highly concentrated and confined in the graphene layers, which results from the excitation of Fabry-Pérot resonances in multi-layer structures. It should be noted that the strongest absorption occurs in the first graphene layer regardless of the number of graphene/silica units, which is consistent with the concentrated electric field distribution, indicating the important role of the top graphene layer in microwave absorption.

Furthermore, the enhanced absorption at the off-resonant frequencies, which contributes to the broadband absorption behavior, is attributed to the modulated electric field intensities
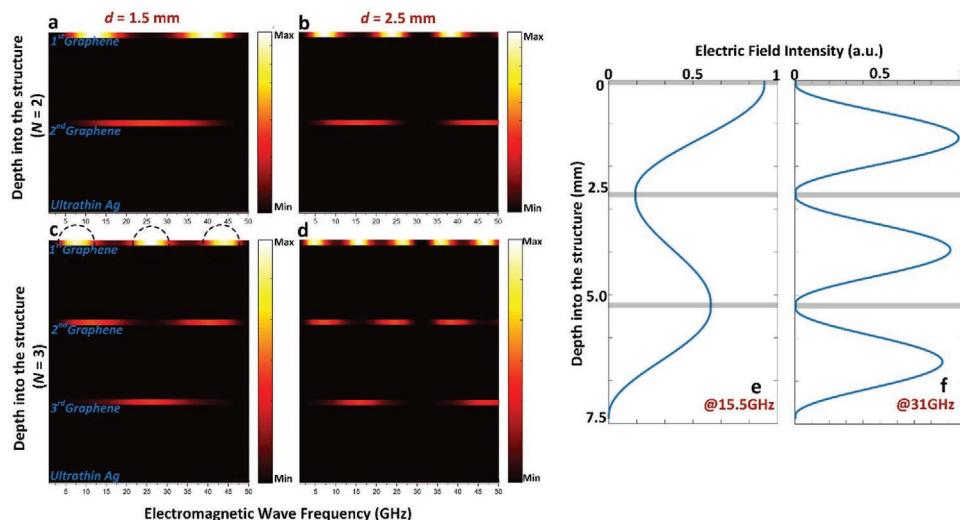
**ADVANCED
SCIENCE NEWS**
www.advancedsciencenews.com

**ADVANCED
MATERIALS
INTERFACES**
www.advmatinterfaces.de

**Figure 6.** Simulated microwave absorption distributions in the structures at different frequencies. a) $d = 1.5$ mm, $N = 2$. b) $d = 2.5$ mm, $N = 2$. c) $d = 1.5$ mm, $N = 3$. d) $d = 2.5$ mm, $N = 3$. e,f) Calculated electric field intensity into the MGSS ($d = 2.5$ mm, $N = 3$) at absorption peak (15.5 GHz) and valley (31 GHz).

in the second and third graphene layers, as shown in Figure 5. The energy absorption in the second and third graphene layers primarily work on the off-resonant frequencies, which is complementary to the first graphene layer in terms of microwave absorption. By adding more graphene/silica units, multiple Fabry-Pérot resonances can be created at different frequencies, which intensifies the electric field distributions in the top graphene layer and promotes electric field levels in other graphene layers, thus extending the absorption bandwidth with high absorption efficiency. Therefore, by employing multiple graphene/silica units, we proved that a broader bandwidth can be obtained with favorable efficiency.

To understand the underlying absorption insights more intuitively, we investigated the electric field intensity profile of the MGSS ($d = 2.5$ mm, $N = 3$) at the absorption peak (@15.5 GHz) and valley (@31 GHz), respectively. As shown in Figure 6e,f, the electric fields in the three graphene layers (gray areas) are all close to zero at the absorption valley, in contrast to the relatively high field strength at the absorption peaks. Based on the results in Figures 5 and 6, it is clear that each of the graphene layers is responsible for the high-efficiency broadband absorption, among which the top layer is of vital importance for absorbing most of the energy at specific resonant frequencies, and the additional graphene layers help improve the off-resonant absorption, which shows a complementary absorption effect with the top graphene layer.

### 2.4. Effect of Graphene Properties on Microwave Absorption

Graphene, which is confirmed to be a microwave-absorbing layer in multi-layer structures, plays a vital role in the overall absorption performance. In general, the conductivity of graphene is the key parameter that contributes to energy absorption or dissipation, which determines the quality of graphene, and it shows an almost linear relationship with its Fermi energy level.[50–54] First, we examine how the graphene properties affect microwave

absorption performance using few-layer and multi-layer graphene instead of monolayer graphene used in previous experiments to construct multi-layer cavities. Confocal laser scanning microscopy (CLSM) and AFM images of CVD-grown graphene films at different layer numbers are shown in Figure S5, Supporting Information, with clear wrinkles on the graphene films because of the different thermal expansion coefficients between the film and substrate. Compared to monolayer graphene, few- to multi-layer graphene have lower electrical conductivities owing to growth defects. The measured averaged sheet resistance of the samples using four-point probe method is 944.3 Ω $\square^{-1}$, 1.07 kΩ $\square^{-1}$, and 1.43 kΩ $\square^{-1}$, respectively, validating the decreasing trend of the electrical conductivity with the increase of graphene layers.

Subsequently, we measured the microwave absorption of the MGSS in the Ku band from $N = 1$ to $N = 3$ at different dielectric thicknesses, as shown in **Figure 7**a–c. For multi-layer cavities at the same $N$ and $d$, few- to multi-layer graphene cavities showed a slight decrease in absorption efficiencies in contrast to the monolayer cavities. It is interesting to note that the influence gradually weakens as the number of units increases, and at the resonant frequencies, all multi-layer structures for $N \geq 2$ can reach a maximum absorption efficiency of ≈99%, except for a small frequency shift. It provides more degrees of freedom to employ graphene within a certain range of electrical conductivities, all contributing to a favorable absorption efficiency, particularly for $N \geq 2$. In addition, the monolayer graphene offers the lowest optical loss in the visible range, and the measured visible transmittance is higher than that of the few-layer to multi-layer graphene. Therefore, the adoption of monolayer graphene is the best choice for improving absorption efficiency and transparency.

Furthermore, as the Fermi level of graphene can be changed by applying a biased voltage, it provides an active and controllable method to tune the microwave absorption, absorption bandwidth, and modulation depth of the MGSS.[55–57] As shown in Figure S6, Supporting Information, the calculated peak
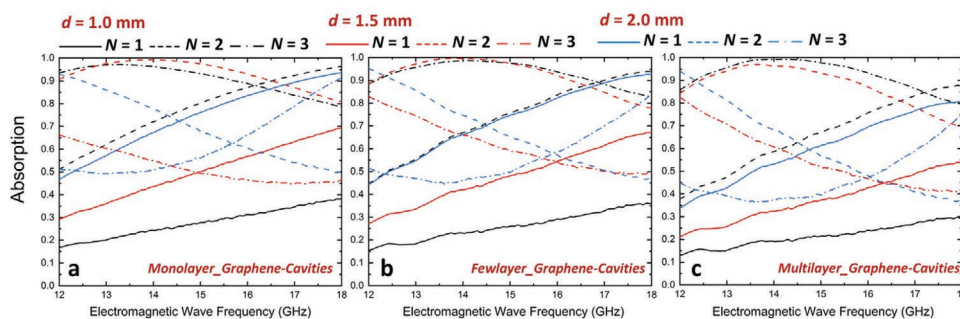
**ADVANCED
SCIENCE NEWS**
www.advancedsciencenews.com

**ADVANCED
MATERIALS
INTERFACES**
www.advmatinterfaces.de

**Figure 7.** Measured microwave absorption of the multi-layer structures in the Ku band composed of different graphene. a) Monolayer graphene. b) Few-layer graphene. c) Multi-layer graphene.

absorption of the MGSS varied at different Fermi levels, and a bandwidth of over-90% absorption can also be improved.

## 2.5. Optical Properties of the MGSS

Finally, we examined the optical properties of multi-layer structures consisting of monolayer graphene, silica, and ultrathin Ag films. It is worth noting that the dielectric thickness of the MGSS we used is on the order of several millimeters, which is far beyond the wavelength of visible light; hence, the incident light could not meet the coherent condition. Therefore, the visible transparency of the MGSS depends on the number of graphene/silica units, and more units decrease the optical transmittance by introducing more absorption (graphene layers) and increasing the interface reflection loss. As can be observed from **Figure 8**, the measured curves show similar trends as predicted. The measured average visible transmittance (400–700 nm) of the MGSS ($d = 1$ mm) were ≈85.8%, 76.5%, and 68.0% for $N = 1$, $N = 2$, and $N = 3$, respectively.

Each monolayer graphene results in ≈2.3% optical loss, and the additional loss comes from silica/air and air/graphene interfaces when adding more pairs, which results from interface

reflection loss owing to mismatched refractive index. In addition, each curve in the figure exhibits a downward trend from the visible to the near-infrared range because of the ultrathin Ag layer, the optical reflection of which continues to increase with increasing wavelength. For MGSS with thicker dielectrics, the optical property is similar to that of silica, which has negligible optical absorption loss ($\kappa \approx 0$). The inset in Figure 8 presents a photograph of the fabricated MGSS at $d = 1.0$ mm, through which the logo can be clearly observed, showing great visible transparency. Figure S7, Supporting Information shows photographs of the fabricated MGSS samples composed of few-and multi-layer graphene as a replacement for monolayer graphene, and it is clear that the visual transparency of the multi-layer structures drops significantly, especially when $N \geq 2$.

## 2.6. Comparison

**Table 1** presents the optical and microwave absorption performances of recently reported representative transparent microwave absorbers. The MGSS prepared in this study showed an excellent absorption bandwidth ($A \geq 50\%$) with a peak absorption efficiency of near unity, indicating its slow downward trend
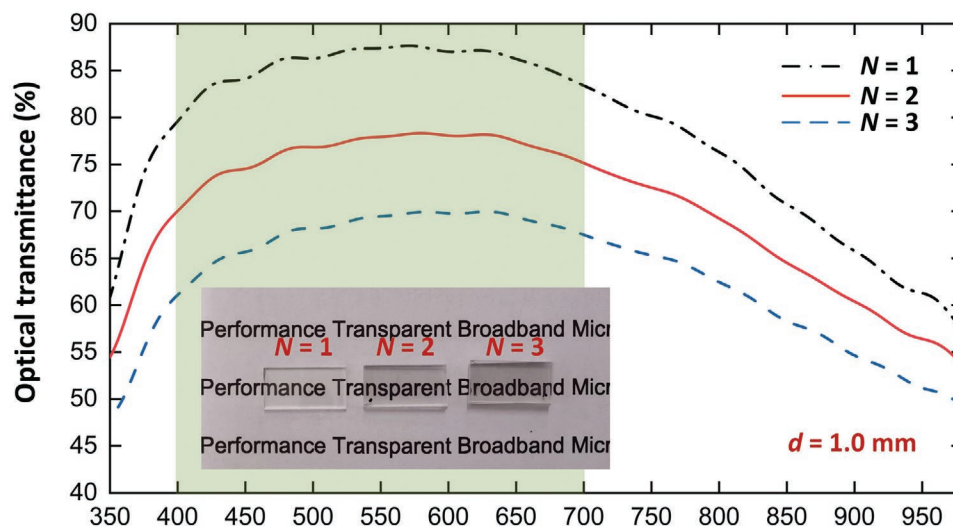


**Figure 8.** Measured optical transmittance of the multi-layer structures from $N = 1$ to $N = 3$ at silica thicknesses $d = 1.0$ mm. Inset is the photograph of the MGSS samples.

**ADVANCED
SCIENCE NEWS**

www.advancedsciencenews.com

**ADVANCED
MATERIALS
INTERFACES**

www.advmatinterfaces.de

**Table 1.** Optical and microwave absorption properties of different microwave absorbers.

| Microwave absorbers | Peak absorption | Absorption bandwidth [GHz] | | Absolute transmittance | Ref. |
|---|---|---|---|---|---|
| | | $A \geq 50\%$ | $A \geq 90\%$ | | |
| Monolayer CVD graphene | ≈40% | 0 | 0 | – | Hong et al.[58] |
| PEI/RGO (2 layers) | 48.26% | 0 | 0 | 62% | Kim et al.[59] |
| Graphene/PET (4 layers) | 86.69% | 8.5 | 0 | – | Lu et al.[33] |
| Graphene/PET (8 layers) | 95.82% | 8.5 | 5.5 | – | Lu et al.[33] |
| Graphene FSS (FTMA) | ≈90% | 14 | 9 | ≈70% | Lu et al.[24] |
| Patterned graphene | ≈100% | 6 | ≈1.5 | 80% | Yi et al.[60] |
| Wheel-like metasurface | ≈100% | 14 | 10.5 | 65–80% | Deng et al.[61] |
| ITO-based metamaterial | ≈99% | ≈25 | ≈10 | – | Lai et al.[62] |
| Windmill-shaped ITO | >95% | 10 | 9.1 | 77% | Zhang et al.[13] |
| ITO resistive films | ≈95% | 14 | 7 | <75% | Sheokand et al.[14] |
| Closed-ring resonators | >95% ($TE_x$) ≈62% ($TM_x$) | ≈24 ($TE_x$) ≈10 ($TM_x$) | 14 0 | ≈82% | Hu et al.[17] |
| Bow-tie Al-mesh | ≈98% | 8 | 6 | 62% | Jang et al.[20] |
| Printed metal mesh | >99% | ≈7 | 4.28 | 81.3% | Lee et al.[63] |
| MGSS ($d = 1$ mm, $N = 2$) | ≈99.5% | 30 | 7.5 | ≈76.5% | This study |
| MGSS ($d = 1$ mm, $N = 3$) | ≈99.5% | 28 | ≈10 | ≈68% | This study |

from the peak absorption by rational design compared to other resonant metamaterial/metasurface structures, which results from the lowered quality factor of single absorption resonance and the enhanced off-resonant absorption by the introduced additional graphene layers and has unique advantages in practical applications. Furthermore, when we consider the criteria of $A \geq 90\%$ as a comparison, the measured effective absorption bandwidth of MGSS ($d = 1$ mm, $N = 2$) is ≈7.5 GHz, and it further extends to ≈10 GHz for the MGSS ($d = 1$ mm, $N = 3$), which still performs well among the transparent microwave absorbers.

## 3. Conclusions

In this study, a multi-layered structure consisting of graphene/silica units and ultrathin Ag films for transparent broadband microwave absorbers has been demonstrated. We present the design guidelines to achieve broadband absorption and reveal the complementary effect of different graphene layers on the microwave absorption mechanism in multi-layer structures for the first time. The experimental results are consistent with the theoretical calculations, and the broadband absorption physical mechanisms can be explained by the excitation of the multi-cavity Fabry-Pérot resonances. The experimental results show that the MGSS ($d = 1$ mm, $N = 2$) presents an absorption bandwidth ($A \geq 50\%$) of ≈30 GHz in the measured 32-GHz-band, peak absorption of ≈99%, and an average visible transmittance of ≈76.5%. Furthermore, the peak absorption efficiency and bandwidth, as well as resonant frequencies, can be easily

tuned by utilizing different numbers of graphene/silica units or simply altering the silica thickness. It is thus expected that a much broader absorption can be achieved by inserting more pairs of graphene/dielectric, thereby opening the door to a multitude of new applications for transparent microwave absorbing materials.

## 4. Experimental Section

*Graphene Synthesis*: The graphene films were grown on copper foil (Alfa Aesar, 40-μm-thick, 99.8% purity) in a quartz tube furnace using the CVD method; the foil was first heated to 1000 °C under $H_2$ atmosphere for 50 min. Then, $CH_4$ gas was introduced into the quartz tube for ≈2 h. The furnace was then cooled to room temperature in the $H_2$ and $CH_4$ mixed gas, and the gas flow was adjusted to 30 and 0.5 mL min$^{-1}$, respectively. After annealing for 30 min, the graphene-coated copper foils were removed from the furnace.

*Graphene Transfer*: PMMA was used as a polymer support for graphene transfer. The specific steps can be described as follows: Step 1 was intended for coating PMMA on the graphene/Cu surface with 30-μL PMMA solutions (4 wt%) dropped on the as-grown sample, spin-coated at 2500 rpm for ≈30 s, and cured on a hotplate at 150 °C for 3 min; Step 2, remove the Cu film by etching the PMMA/graphene/Cu sample using FeCl$_3$ solution (0.05 g mL$^{-1}$) for ≈12 h until complete dissolution of Cu metals was achieved. In this step, clean deionized water solution was repeatedly added to replace the etching solution to ensure the maximal removal of other ionic impurities remaining on the film surface; Step 3 was the final stage to transfer floating PMMA/graphene onto the target quartz substrate, which was realized by inclining the sample and drying it naturally. Subsequently, the PMMA/graphene/quartz sample was dipped into the acetone solution for ≈4 h to further remove PMMA, followed by the standard washing and drying processes.

*Device Fabrication*: Ultrathin Ag films were deposited using co-sputtering method from Cu and Ag targets with the deposition rate being 0.19 and 11.09 Å s$^{-1}$, respectively, leading to ≈2% atomic concentration of Cu in the obtained film. The Ag film thickness was controlled by the deposition rate and deposition time, which were calibrated using an ellipsometer. It should be mentioned that considering the strong optical reflection of the ultrathin Ag film, 40-nm-thick ITO was coated as optical antireflection layers on both sides of as-grown 8-nm-thick ultrathin Ag to simultaneously improve visible transmittance and electrical conductivity. ITO antireflection coatings for ultrathin Ag films were deposited using radiofrequency magnetron sputtering at a rate of 50 nm min$^{-1}$. Finally, MGSS samples were prepared by stacking the graphene/quartz units and ultrathin Ag films according to the different configurations, and different units were bonded by 100-μm-thick optical clear adhesion (OCA, Sanling Co.) between the layers. To make adjacent units adhere more closely and remove small bubbles, a silicone roller was employed to repeatedly roll on the samples until the device became a whole structure.

*Characterization and Measurements*: The surface morphologies of the graphene and ultrathin Ag films were investigated using SEM (Nikon SMZ1500), tapping mode AFM (Bruker Dimension), and CLSM (Olympus LEXT OLS5100), respectively. Raman spectra of the graphene films were measured using a Raman spectrometer (HORIBA, LabRAM XploRA) and are shown in Figure S8, Supporting Information. XPS spectra were performed by Escable 250Xi (Thermo Scientific) using Al K$\alpha$ radiation (1486.6 eV), and binding energies were calibrated to the C 1s value at 284.6 eV. Sheet resistances were measured using a four-point probe method with an ST2263 double testing digital four-probe tester, and the results were the average values from three different domains of each sample. The microwave transmission and reflection of the samples at different configurations were measured by waveguide methods using a vector network analyzer (KEYSIGHT N5234A) in the X, Ku, K, and Ka bands. The graphene, silica, and ultrathin Ag films were cut into different dimensions to precisely fit the waveguides for the measurements in different bands (X band: 22.7 × 10 mm$^2$, Ku band: 15.6 × 7.7 mm$^2$, K band: 10.5 × 4.2 mm$^2$, and Ka band: 7.0 × 3.4 mm$^2$). The incoming electromagnetic waves were normally incident on the test samples. The optical transmittance of the samples at different configurations was characterized using a UV–Vis-infrared spectrophotometer (PerkinElmer Lambda 950) at normal incidence.

## Supporting Information

Supporting Information is available from the Wiley Online Library or from the author.

## Acknowledgements

## Conflict of Interest

The authors declare no conflict of interest.

## Data Availability Statement

Research data are not shared.

[1] F. Shahzad, M. Alhabeb, C. Hatter, B. Anasori, S. Hong, C. Koo, Y. Gogotsi, *Science* **2016**, *353*, 1137.
[2] P. Kumar, *Adv. Mater. Interfaces* **2019**, *6*, 1901454.
[3] H. Wang, Y. Zhang, C. Ji, C. Zhang, D. Liu, Z. Zhang, Z. Lu, J. Tan, L. J. Guo, *Adv. Sci.* **2019**, *6*, 1901320.
[4] J. Huang, T. Wang, Y. Su, Y. Ding, C. Tu, W. Li, *Adv. Mater. Interfaces* **2021**, *8*, 2100186.
[5] M. Yang, Q. Wei, J. Li, Y. Wang, H. Guo, L. Gao, L. Huang, X. He, Y. Li, Y. Yuan, *Adv. Mater. Interfaces* **2020**, *7*, 1901815.
[6] T. Almoneef, O. Ramahi, *Appl. Phys. Lett.* **2015**, *106*, 153902.
[7] Y. Han, Y. X. Liu, L. Han, J. Lin, P. Jin, *Carbon* **2017**, *115*, 34.
[8] Z. Lu, L. Ma, J. Tan, H. Wang, X. Ding, *2D Mater.* **2017**, *4*, 025021.
[9] R. Deng, K. Zhan, M. Li, L. Song, T. Zhang, *Mater. Des.* **2018**, *162*, 119.
[10] D. Yoo, D. Won, W. Cho, J. Lim, J. Kim, *Adv. Mater. Technol.* **2021**, 2100358.
[11] S. Lai, Y. Wu, X. Zhu, W. Gu, W. Wen, *IEEE Photonics J.* **2017**, *9*, 1.
[12] H. Sheokand, G. Singh, S. Ghosh, J. Ramkumar, S. Ramakrishna, K. Srivastava, *IEEE Antennas Wireless Propag. Lett.* **2019**, *18*, 113.
[13] C. Zhang, Q. Cheng, J. Yang, J. Zhao, T. Cui, *Appl. Phys. Lett.* **2017**, *110*, 722.
[14] H. Sheokand, S. Ghosh, G. Singh, M. Saikia, K. Srivastava, J. Ramkumar, S. Ramakrishna, *J. Appl. Phys.* **2017**, *122*, 105105.
[15] J. Zhao, C. Zhang, Q. Cheng, J. Yang, T. Cui, *Appl. Phys. Lett.* **2018**, *112*, 073504.
[16] K. Chen, L. Cui, Y. J. Feng, J. Zhao, T. Jiang, B. Zhu, *Opt. Express* **2017**, *25*, 5571.
[17] D. Hu, J. Cao, W. Li, C. Zhang, T. Wu, Q. Li, Z. Chen, Y. Wang, J. Guan, *Adv. Opt. Mater.* **2017**, *5*, 1700109.
[18] H. Xiong, J. Hong, C. Luo, L. Zhong, *J. Appl. Phys.* **2013**, *114*, 064109.
[19] F. Ding, Y. Cui, X. Ge, Y. Jin, S. L. He, *Appl. Phys. Lett.* **2012**, *100*, 103506.
[20] T. Jang, H. Youn, Y. J. Shin, L. J. Guo, *ACS Photonics* **2014**, *1*, 279.
[21] P. Min, Z. Song, L. Yang, B. Dai, J. Zhu, *Opt. Express* **2020**, *28*, 19518.
[22] Q. Zhou, X. Yin, F. Ye, R. Mo, Z. Tang, X. Fan, L. Cheng, L. Zhang, *Appl. Phys. A: Mater. Sci. Process.* **2019**, *125*, 131.
[23] Y. Wu, J. Wang, S. Lai, X. Zhu, W. Gu, *AIP Adv.* **2019**, *9*, 025309.
[24] W. Lu, J. Wang, J. Zhang, Z. Liu, H. Chen, W. Song, Z. Jiang, *Carbon* **2019**, *152*, 70.
[25] H. Chen, W. Lu, Z. Liu, J. Zhang, A. Zhang, B. Wu, *IEEE Trans. Microwave Theory Tech.* **2018**, *66*, 3807.
[26] O. Balci, E. Polat, N. Kakenov, C. Kocabas, *Nat. Commun.* **2015**, *6*, 6628.
[27] M. Grande, G. Bianco, M. Vincenti, D. Ceglia, P. Capezzuto, V. Petruzzelli, M. Scalora, G. Bruno, A. D'Orazio, *Opt. Express* **2016**, *24*, 22788.
[28] H. Chen, W. Ma, Z. Huang, Y. Zhang, Y. Huang, Y. Chen, *Adv. Opt. Mater.* **2019**, *7*, 1801318.
[29] B. Wu, H. Tuncer, A. Katsounaros, W. Wu, M. Cole, K. Ying, L. Zhang, W. Milne, Y. Hao, *Carbon* **2014**, *77*, 814.
[30] K. Zhang, J. Zhang, Z. Hou, S. Bi, Q. Zhao, *Carbon* **2019**, *141*, 608.
[31] D. Yi, X. Wei, Y. Xu, *IEEE Trans. Microwave Theory Tech.* **2017**, *65*, 2819.
[32] Y. Bai, B. Zhong, Y. Yu, M. Wang, J. Zhang, B. Zhang, K. Gao, A. Liang, C. Wang, J. Zhang, *npj 2D Mater. Appl.* **2019**, *3*, 32.

[33] Z. Lu, L. Ma, J. Tan, H. Wang, X. Ding, *Nanoscale* **2016**, *8*, 16684.

[34] K. Batrakov, P. Kuzhir, S. Maksimenko, A. Paddubskaya, S. Voronovich, P. Lambin, T. Kaplas, Y. Svirko, *Sci. Rep.* **2014**, *4*, 7191.

[35] B. Wu, H. Tuncer, M. Naeem, B. Yang, M. Cole, W. Milne, Y. Hao, *Sci. Rep.* **2014**, *4*, 4130.

[36] Y. Chang, C. Liu, C. Liu, S. Zhang, S. Marder, E. Narimanov, Z. Zhong, T. Norris, *Nat. Commun.* **2016**, *7*, 10568.

[37] I. Iorsh, I. Mukhin, I. Shadrivov, P. Belov, Y. Kivshar, *Phys. Rev. B: Condens. Matter Mater. Phys.* **2013**, *87*, 075416.

[38] M. Othman, C. Guclu, F. Capolino, *Opt. Express* **2013**, *21*, 7614.

[39] L. Wang, Z. Ma, Y. Zhang, L. Chen, D. Cao, J. Gu, *SusMat* **2021**, *1*, 413.

[40] F. Qi, L. Wang, Y. Zhang, Z. Ma, H. Qiu, J. Gu, *Mater. Today Phys.* **2021**, *21*, 100512.

[41] L. Wang, X. Shi, J. Zhang, Y. Zhang, J. Gu, *J. Mater. Sci. Technol.* **2020**, *52*, 119.

[42] H. Y. Wang, C. G. Ji, C. Zhang, Y. L. Zhang, Z. Zhang, Z. G. Lu, J. B. Tan, L. J. Guo, *ACS Appl. Mater. Interfaces* **2019**, *11*, 11782.

[43] C. Zhang, Q. Y. Huang, Q. Y. Cui, C. G. Ji, Z. Zhang, X. Chen, T. George, S. L. Zhao, L. J. Guo, *ACS Appl. Mater. Interfaces* **2019**, *11*, 27216.

[44] C. Zhang, C. Ji, Y. B. Park, L. J. Guo, *Adv. Opt. Mater.* **2020**, *9*, 2001298.

[45] A. Siokou, F. Ravani, O. F. S. Karakalos, M. Kalbac, C. Galiotis, *Appl. Surf. Sci.* **2011**, *257*, 9785.

[46] R. Stine, J. W. Ciszek, D. E. Barlow, W. K. Lee, J. T. Robinson, P. E. Sheehan, *Langmuir* **2012**, *28*, 7957.

[47] X. Gao, S. Wang, J. Li, Y. Zheng, R. Zhang, P. Zhou, Y. Yang, L. Chen, *Thin Solid Films* **2004**, *455*, 438.

[48] Z. Yang, Y. Chen, Y. Zhou, Y. Wang, P. Dai, X. Zhu, H. Duan, *Adv. Opt. Mater.* **2017**, *5*, 1700029.

[49] Z. Li, E. Palacios, S. Butun, H. Kocer, K. Aydin, *Sci. Rep.* **2015**, *5*, 15137.

[50] L. Zhu, F. Liu, H. Lin, J. Hu, Z. Yu, X. Wang, S. Fan, *Light: Sci. Appl.* **2016**, *5*, e16052.

[51] L. Jia, D. Yan, X. Liu, R. Ma, H. Wu, Z. Li, *ACS Appl. Mater. Interfaces* **2018**, *10*, 11941.

[52] Y. G. Bi, Y. F. Liu, X. L. Zhang, D. Yin, W. Q. Wang, J. Feng, H. B. Sun, *Adv. Opt. Mater.* **2019**, *7*, 1800778.

[53] X. Liang, J. Lu, T. Zhao, X. Yu, Q. Jiang, Y. Hu, P. Zhu, R. Sun, C. P. Wong, *Adv. Mater. Interfaces* **2019**, *6*, 1801635.

[54] J. Lu, Y. Zhang, Y. Tao, B. Wang, W. Cheng, G. Jie, L. Song, Y. Hu, *J. Colloid Interface Sci.* **2020**, *588*, 164.

[55] S. K. Guo, J. Deng, J. Zhou, Y. Yu, Y. Bu, T. Zhu, X. Ren, Z. Li, W. Lu, X. Chen, *Opt. Express* **2021**, *29*, 9269.

[56] Y. Yu, J. Zhou, Q. Cai, Z. Chu, J. Deng, W. Lu, Z. Li, X. Chen, *Opt. Lett.* **2021**, *46*, 2236.

[57] S. Guo, D. Zhang, J. Zhou, J. Deng, Y. Yu, J. Deng, Q. Cai, Z. Li, W. Lu, X. Chen, *Carbon* **2020**, *170*, 49.

[58] S. Hong, K. Kim, T. Kim, J. Kim, S. Park, J. Kim, B. Cho, *Nanotechnology* **2012**, *23*, 455704.

[59] S. Kim, J. Oh, M. Kim, W. Jang, M. Wang, Y. Kim, H. Seo, Y. Kim, J. Lee, Y. Lee, J. Nam, *ACS Appl. Mater. Interfaces* **2014**, *6*, 17647.

[60] D. Yi, X. C. Wei, Y. Xu, *IEEE Trans. Nanotechnol.* **2017**, *16*, 484.

[61] R. Deng, K. Zhang, M. Li, L. Song, T. Zhang, *Mater. Des.* **2019**, *162*, 119.

[62] S. Lai, Y. Wu, X. Zhu, W. Gu, W. Wu, *IEEE Photonics J.* **2017**, *9*, 1.

[63] I. Lee, S. Yoon, J. Lee, I. Hong, *Electron. Lett.* **2016**, *52*, 555.